METHODS • OPEN ACCESS

Method—Multi-Cell Testing with Active Driven Gas Layer Concept: Advantages and Limitations

To cite this article: Y. Liu *et al* 2024 *J. Electrochem. Soc.* **171** 104509

View the article online for updates and enhancements.

Method—Multi-Cell Testing with Active Driven Gas Layer Concept: Advantages and Limitations

Y. Liu,[1,z] Y. Hu,[2] M. Juckel,[3] N. H. Menzler,[3] and A. Weber[1,*]

[1]Institute for Applied Materials (IAM-ET), Karlsruhe Institut of Technologie (KIT), Karlsruhe 76131, Germany
[2]Institute of Energy Materials and Devices (IMD), IMD-1: Structure and Function of Materials, Forschungszentrum Jülich GmbH, Jülich 52425, Germany
[3]Institute of Energy Materials and Devices (IMD), IMD-2: Materials Synthesis and Processing, Forschungszentrum Jülich GmbH, Jülich 52425, Germany

This study validates a novel method for simultaneous durability testing of multiple symmetrical cells with Ni/ceria fuel electrodes. The investigation demonstrates that gas diffusion losses in the multi-cell test setup utilizing the active driven gas layer concept have a smaller impact on cell performance compared to the single-cell setup. This method proves effective for testing multiple identical cells, offering a time and cost-efficient approach. However, testing symmetrical cells with different fuel electrodes reveals an unexpected pseudo-inductive loop in the impedance spectra, observable only in the multi-cell setup. Analysis of impedance spectra and relaxation times indicates that differences in electrode polarization resistance result in varying gas compositions at the two electrodes of a cell, disrupting symmetry and superimposing an additional Nernst voltage term. To understand this, an electrical equivalent circuit model with the Nernst voltage term was developed to reproduce the observed behavior. Comparison of experimental and simulation results substantiates the model and elucidates the mechanisms. The findings indicate that testing multiple cells with the active driven gas layer concept is applicable only for identical cells and not for those with different electrodes.

List of Symbols

|	
A	active area of electrode (m^2)
C_i	the chemical capacitance of cell i (F)
d	the thickness of Ni-mesh (m)
F	Faraday constant (As mol^{-1})
H_2	hydrogen
H_2O	steam
He	helium
HF_j	jth high frequency process
i	ac-current (A)
I	amplitude of ac-current (A)
I_{R_i}	current flowing through the charge transfer resistance of cell i (A)
j	imaginary unit
LF_j	jth low frequency process
LF_x	the low frequency process related to pseudo-inductive loop
MF_j	jth middle frequency process
$m_{H_2,m.(n)}$	mole mass of hydrogen at position (n) (n = 1,2) of cell m (m = 1–3) (mol)
$m_{H_2,mn}$	mole mass of hydrogen in the "sealed" space between cell n and m (m, n = 1–3) (mol)
$m_{H_2O,m.(n)}$	mole mass of steam at position (n) (n = 1,2) of cell m (m = 1–3) (mol)
$m_{H_2O,mn}$	mole mass of steam in the "sealed" space between cell n and m (m, n = 1–3) (mol)
$m_{i,preset}$	preset mole mass of component i (H$_2$/ H$_2$O) in the "sealed" space between cells (mol)
m_{sealed}	total mole mass of gas mixture in the "sealed" space between cells (mol)
N_2	nitrogen
$Ni(NO_3)_3$	nickel nitrate
O_2	oxygen
P	total pressure of gas in the test chamber (atm)
p_{H_2}	hydrogen partial pressure (atm)
p_{H_2O}	steam partial pressure (atm)
$p_{O_2,bottom\ electrode}$	oxygen partial pressure at bottom electrode of cell (atm)
$p_{O_2,top\ electrode}$	oxygen partial pressure at top electrode of cell (atm)
R	universal gas constant 8.314 (J mol^{-1} K^{-1})
R_i	the charge transfer resistance of cell i (Ω)
t	time (s)
T	temperature (K)
$U_{2,mea}$	measured voltage of cell 2 (V)
U_N	Nernst voltage (V)
Ω	angular velocity (rad/s)
x_i	mole fraction of component i (H$_2$/ H$_2$O) (−)
$Z_{2,mea}$	measured impedance of cell 2 (Ω)
$Z_{2,mea,sim}$	simulated impedance of cell 2 (Ω)
ε	porosity (−)

Durability testing of solid oxide fuel cells (SOFCs) is crucial for achieving expected lifetimes of up to 100,000 h, yet it poses significant challenges during cell and stack development. Extensive long-term tests are preferable to quantify degradation rates, but they are often deemed impractical. Accelerated lifetime tests (ALT) offer a promising solution by enabling faster degradation analysis and reducing testing duration. Carefully designed ALT protocols can provide essential input for degradation models, facilitating simulative durability analysis within a shorter timeframe.[1–4] However, the complex relationship between stressors and degradation mechanisms adds layers of complexity to the analysis. Researchers have observed substantial discrepancies between estimated and actual lifetimes, underscoring the need to deconvolute distinct degradation mechanisms over time.

Efforts have been undertaken to reduce both the time and the number of tests while ensuring the reliability of the obtained results. Simultaneous testing of a larger number of cells in a single test setup can improve statistics and further on enable a comparison of different variants. Such test can be performed in a rainbow stack,[5]

*Electrochemical Society Member.
zE-mail: yanting.liu@kit.edu
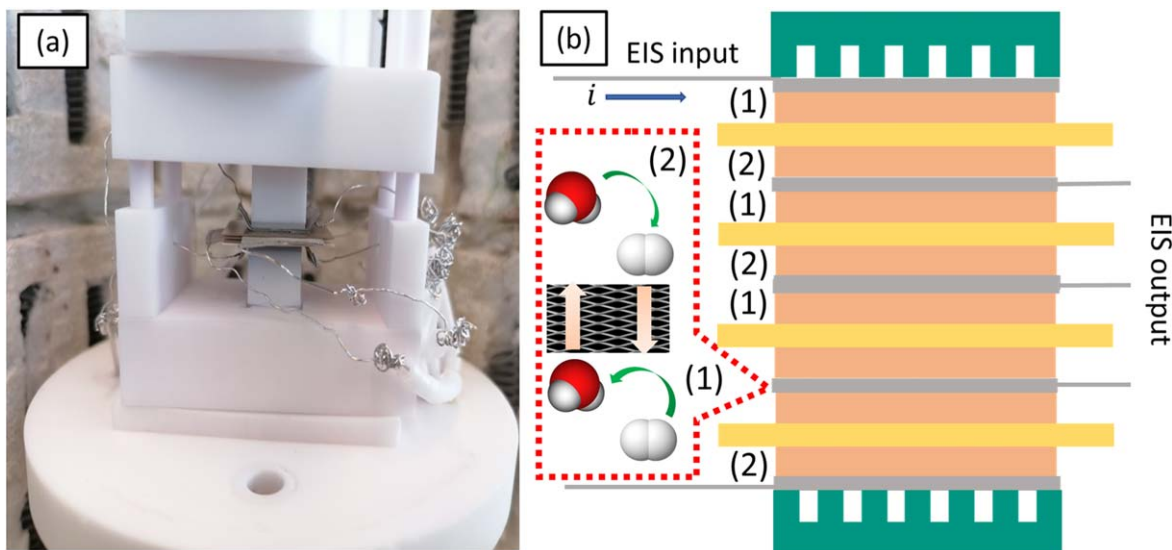
Figure 1. (a) Photograph of the sample holder featuring weights on top and integrated cells. (b) Schematic representation of the multi-cell test setup applying active driven gas layer concept.

which requires an expensive stack production and includes the risk that a faulty cell may accelerate the aging of the other cells. Another approach is testing of multiple cells in a single chamber setup with an appropriate sample holder. Since there is just a single gas composition at all electrodes, this approach is limited to symmetrical cells. One example for an innovative testing method for coupled electrochemical and microstructural life testing is given in.[6] The approach involved the implementation of current switching operations on six parallel connected symmetrical Solid Oxide Cells (SOCs). To assess microstructural and chemical changes over time, cells were removed from the test bench one after the other and analyzed. However, it was observed that the applied silver current collector affected the durability of the electrodes.

For a similar purpose, we developed and implemented a test method that enables simultaneous testing of multiple symmetrical cells in a single gas atmosphere and furthermore minimizes polarization contributions related to gas conversion and diffusion effects by an active driven gas layer concept.[7] The ceramic sample holder, shown in Fig. 1a, enables stacking of multiple cells. Within this stack, highly porous contact-meshes are interposed between the cells and contacted by Pt-wires, allowing for voltage measurement and, in combination with a multiplexer, impedance measurements of each cell in the stack. The various components presented in Fig. 1. (b) merely depict the configuration of the test setup, lacking a definitive scale representation. The ceramic flow field is depicted in green, current collector and associated nickel meshes and wires in grey, the 8 mol% yttria-stabilized zirconia (YSZ) electrolyte in yellow, and the electrode (including the gadolinium-doped ceria (GDC) interlayer) in orange. In the red dialog box, the red ball signifies an oxygen atom, while the white ball represents a hydrogen atom. The light red arrows indicate the direction of gas transport for hydrogen and steam, respectively. The blue arrow denotes the assumed direction of the current flow. Based on that, the positions in one symmetrical cell are marked with (1): $H_2 + O^{2-} \rightarrow H_2O + 2e^-$ and (2): $H_2O + 2e^- \rightarrow H_2 + O^{2-}$. The same applies in Fig. 7. As shown in Fig. 1b, the fuel consumed at one electrode (position (1)) is generated at the electrode of the next cell (position (2)) across the Ni-mesh. This ensures a strictly perpendicular gas transport free from any impact from flow rate and flow field geometry. The top and bottom cells are not considered in the test due to an asymmetrical configuration of distinct gas transport properties at the electrodes. Any kind of glass sealant, ceramic glue or silver paint for fixation, contacting and sealing is avoided. The cells can be contacted by nickel or gold meshes, the contacting is secured

by adding weights onto the sample holder. This modification enhances flexibility in accommodating cells of various sizes and shapes.

In this study, we focus on the validation of this method by electrochemical characterization and durability testing of different Ni/ceria fuel electrodes in symmetrical cells. The investigation of gas diffusion losses in the active driven gas layer (multi-cell) setup revealed that its impact on cell performance is smaller than observed in regular single-cell setups with a stack like in plane gas supply via gas channels.[8] Simultaneous testing of different types of symmetrical cells revealed an unexpected pseudo-inductive loop in the low frequency range of impedance spectra, which was not observable in the regular single cell setup. Investigations into the dependencies of this phenomenon suggests the possibility of an additional voltage contribution resulted from an unmatched amount of components (hydrogen, steam) being consumed or produced between two neighboring electrodes of two neighboring cells. Importantly, the novel test method proved to be excellent for testing multiple identical cells, offering a time and cost-efficient approach. However, its applicability in testing and comparing different cell types is restricted, as the selection of cell types is limited to those exhibiting similar electrochemical behavior.

Experimental

In this work, five distinct Ni/GDC electrodes were investigated in symmetrical electrolyte-supported cells (ESCs), labeled A, B, C, D, and E. Each cell, with an active area (electrode area) of 1 cm², was developed and manufactured at Forschungszentrum Jülich GmbH. All tested cells are based on a 200 μm thick 8YSZ electrolyte (Kerafol, Germany).

After applying GDC paste onto the electrolyte via screen-printing, the cells were sintered at 1300 °C with a heating rate of 3 K min^{-1} and held for 3 h. This sintering process was applied consistently across all cell types. Electrode A was obtained by screen-printing a Ni/GDC layer on top of the GDC layer and sintering it at 1400 °C, resulting in an 8 μm thick Ni/GDC layer.

Cells B to D were produced from electrolytes screen-printed with Ni/GDC paste and sintered at various temperatures, as detailed in Table I.

Cell E was fabricated by first screen-printing and sintering 10 μm thick GDC layers onto the 8YSZ substrate at 1200 °C for 3 h. A Ni catalyst was then introduced via two times of infiltration using a 3 mol/L Ni(NO$_3$)$_2$ solution into the porous GDC skeleton. After each
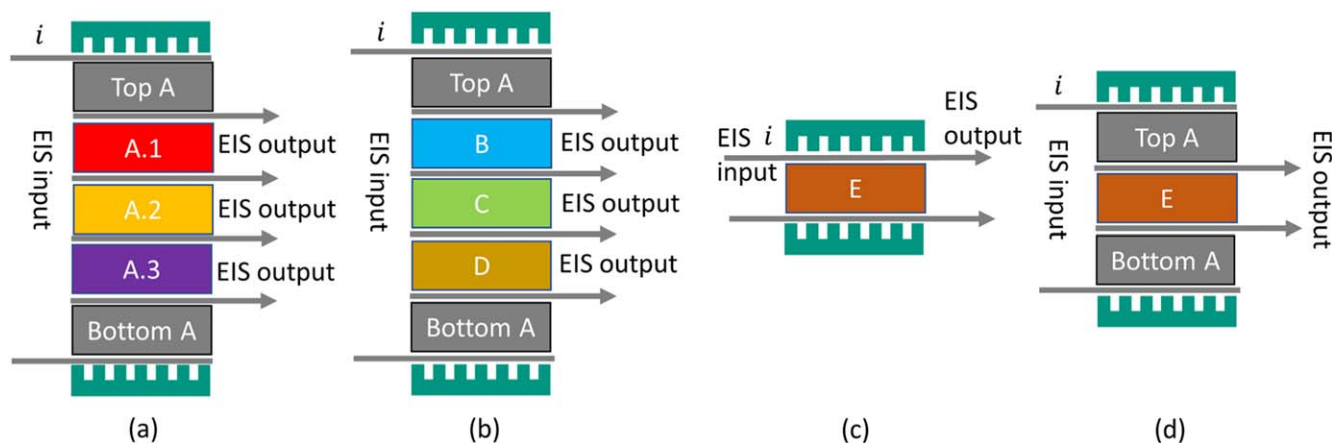
Figure 2. Schematic illustration of tests with (a) identical cells A, (b) different cells B-D, (c) cell E in a regular single-cell test setup, and (d) cell E between two cells A.

Table I. Detailed differences in the cell fabrication process for cell A-E.

Cell type	GDC inter-layer (μm)	Electrode fabrication	Electrode sintering temperature (°C)	Electrode thickness (μm)
A	4	Sintering	1400	8
B		Sintering	1200	10
C		Sintering	1300	10
D		Sintering	1400	8
E		Sintering + Infiltration	1200	10

infiltration step, the cell was dried and heated to 500 °C with a heating rate of 3 K min^{-1}, a dwelling time of 3 h, and a cooling rate of 5 K min^{-1}.

Finally, a NiO paste, forming a Ni contact layer during reduction, was screen printed onto both electrodes of all cells and dried overnight at 90 °C.

The cell stacking and testing method employed in this study are detailed in Ref. 9. For a comprehensive understanding of the test benches, additional information is available in Ref. 10. A total mass flow rate of 500 nlm was set for all the tests carried out with multi-cell test setup in this work. The experimental setup utilized a Solartron 1260 frequency response analyzer with a measurement frequency range spanning from 30 mHz to 1 MHz for electrochemical impedance spectroscopy (EIS), employing 12 points per decade. Each EIS measurement started with two measurements at frequencies of 200,000 Hz and 0.2 Hz. The difference in the real impedance values at these frequencies was estimated the polarization resistance of the cell being tested. The amplitude of the activation signal was then determined by dividing 12 mV by this polarization resistance. The sinusoid activation signal traversed the entire cell stack (EIS input). The Ni meshes with Pt-wires positioned between the cells enabled voltage measurements, as depicted in Fig. 1c in Ref. 9. With a multiplexer, the channel for EIS output can be switched between the cells, enabling a scanning output. All measurements were conducted under open circuit voltage (OCV) conditions to maintain the electrochemical symmetry of the cells. The reliability of the EIS results has been validated by Kramers–Kronig test.

Testing symmetrical cells in such a stack-like arrangement with active driven gas layers supports two different approaches aiming at: (i) increasing statistics and enabling microstructural investigations of samples removed after a well-defined period during a long-term test and (ii) testing the performance and durability of different electrodes/cells simultaneously.

Considering the first approach, three cells of type A were assembled with two additional A cells on the top and bottom (Fig. 2a). The cells were heated in nitrogen up to 800 °C and then gradually reduced in a nitrogen/hydrogen gas mixture for 1 h. Gas composition was adjusted to a 50:50 ratio of water steam to hydrogen by introducing a 0.125 nlm oxygen flow to the combustion humidifier. Initial characterization was carried out on the cells in the center at temperatures of 800, 650, and 600 °C. After cooling down and removing cell A.1, the remaining four cells were heated up to 900 °C and operated for 240 h under the same gas composition. Cell A.2 was then demounted. The remaining cell A.3, along with the top and bottom cells, was heated up to 900 °C and further operated until the total operating time exceeded 1000 h. After the aging test, an inert gas alternating test was performed at 800 °C on cell A.3 to investigate the gas diffusion loss in the multi-cell test setup.

To analyze the capability of investigating different cells simultaneously in this setup, 3+2 cells (3 cells B-D in series, with 2 additional A cells on the top and bottom, as depicted in Fig. 2b) were assembled into the ceramic sample holder. To assess the aging behavior of the different cells, a mid-term aging procedure was conducted at 700 °C for 900 h after initial characterization. Subsequently, impedance spectra were measured under systematically varied operating conditions, including changes in gas composition and inert gas types.

To evaluate differences between a regular single-cell test bench with parallel gas flow at both electrodes and the active driven gas layer (multi-cell) setup, cell type E was initially operated in a single-cell test setup (Fig. 2c) at 600 °C and then sandwiched between two A cells (Fig. 2d) in an active driven gas layer (multi-cell) stack under the same condition.

Results and Discussion

Multicell test with identical cells.—To investigate the difference in gas diffusion loss between a cell inside the stack (with both electrodes in the active driven gas layer mode) and a cell tested in a regular single-cell setup, impedance spectra and corresponding Distribution of Relaxation Times (DRTs) for electrode A.3 with alternating inert gas types are shown in Fig. 3. Three arcs are clearly visible in the Nyquist plot, with two of them being identical when alternating inert gas. The arc at the low-frequency range, although not complete due to the selected frequency range in the measurement, exhibited an obvious decrease when alternating from nitrogen to helium. The corresponding DRTs indicated that the process below 1 Hz is largely depending on the inert gas and thus is most likely a gas diffusion process.[8] The difference in resistance induced by alternating inert gas is estimated to be 0.01 Ωcm^2 by complex nonlinear least squares (CNLS) fit with RQ-elements. This value
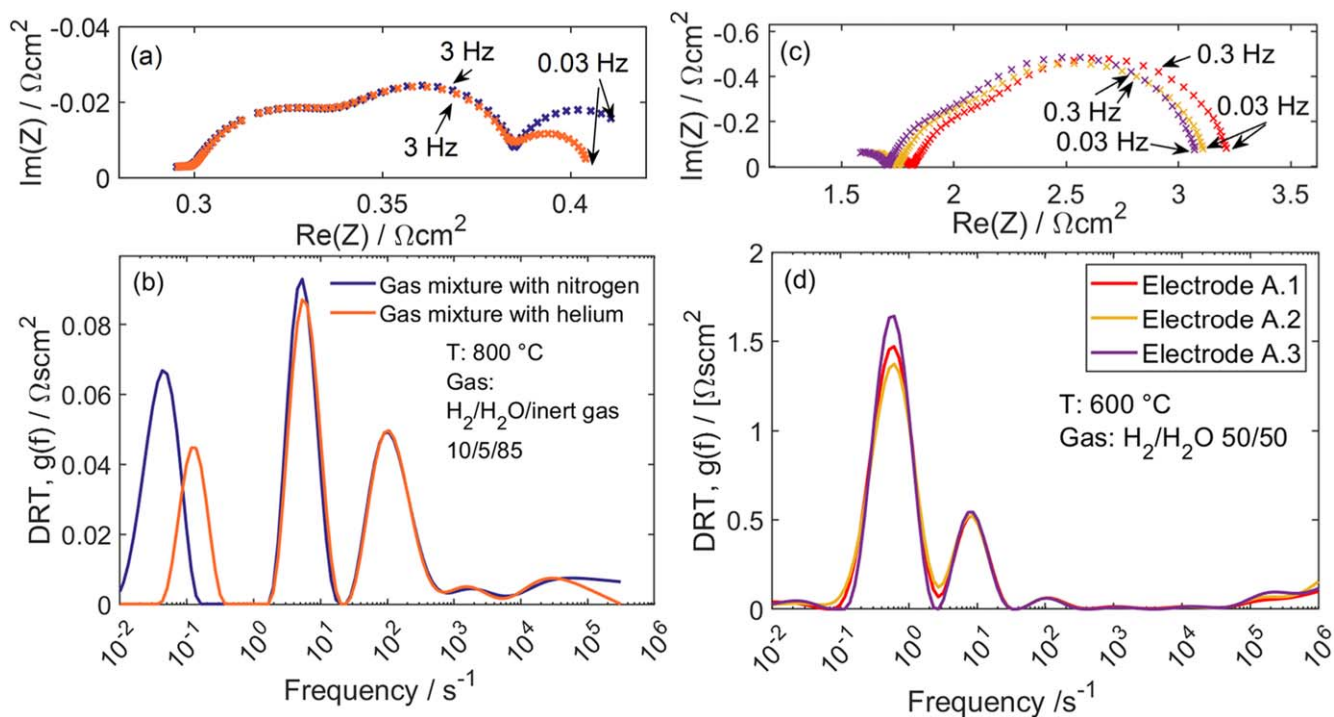
Figure 3. (a) Impedance spectra and (b) corresponding DRTs of electrode A.3 with alternating inert gas (steam and hydrogen partial pressures are 0.05 and 0.30 atm at 800 °C). (c) Impedance spectra and (d) corresponding DRTs of the electrode of 3 cells of type A. In all graphs the impedance values are halved and thus represent a single electrode.

indicates a gas diffusion loss of approximately $0.0075\ \Omega\cdot cm^2$ at 800 °C with a 50:50 water steam to hydrogen gas mixture. Based on the same method in a regular single-cell setup reported in Ref. 8 the gas diffusion resistance under same condition could be $0.0134\ \Omega\cdot cm^2$. Since gas diffusion losses in electrodes are negligible in both cases due to the thinness, the new test method effectively mitigates these losses.

In Figs. 3c, d, the spectra of a single electrode of the three cells A.1–3 at 600 °C, are depicted, revealing ohmic resistances of 1.815, 1.750, and $1.704\ \Omega\cdot cm^2$ and polarization resistances of 1.395, 1.358, and $1.366\ \Omega cm^2$. As to be expected, the three cells with identical electrodes exhibited a quite similar performance. The deviations observed in ohmic and polarization resistances were 6.46% and 2.74%, respectively.

The results of mid-term test under the accelerated stressor test are detailed in Ref. 9. The good reproducibility of the A.1–3 cells was evident regarding mid-term behavior as well and the efficiency of the test method itself is unequivocally established. This approach has the potential to save a considerable budget on gas, energy supply, and time, making it a cost-effective and resource-efficient testing strategy.

Multicell test with different cells.—The other goal of employing such a methodology is to reduce the number of tests by assembling different cells and testing them simultaneously. This approach in principle allows for a direct comparison of performance and aging behavior of different cells in one test.

The initial characterization of electrodes B-D in the setup shown in Fig. 2b is illustrated in Figs. 4a, 4b. In Fig. 4a, the impedance of electrode C has the best electrochemical performance, but exhibits an unusual feature at low frequencies, where the real part of the impedance curves back, resulting in a decrease in measured polarization resistance. The first main peak between 3–100 Hz appears to broaden compared to those in the DRTs of electrode B and D.

The possibility of a measurement artifact was excluded by the characterization after mid-term operation involving alternating inert

gas and variation of partial pressure of steam and hydrogen. As shown in Fig. 4c, a pseudo-inductive loop appeared below 3 Hz in the impedance spectrum of electrode C, when the partial pressure of steam was reduced to 0.05 atm at 700 °C by introducing inert gases as nitrogen or helium. In the DRTs, six visible peaks are identified and labeled as LF_x, LF_1, LF_2, MF_1, HF_1, and HF_2, ranging from low to high frequencies. LF_x is related to the inductive loop. Its contribution in the DRT (negative peak) is considered by the DRT calculation method developed for proton-exchange membrane (PEM) fuel cells.[11] As indicated in,[12] high-frequency processes (HF, >10 kHz) are related to the resistance within the electrolyte and the GDC/YSZ interface and are not influenced by the new features at low frequency range. Thus, they are not further discussed in this work.

In Fig. 4d, at low steam content, the process LF_{1+2} between 10–300 Hz separates into two low-frequency processes, LF_1 and LF_2. By alternating the inert gas, differences in LF_x and LF_{1+2} are observed. Since hydrogen and steam have different diffusion velocities in nitrogen and helium, which both are electrochemically inert, only gas diffusion-related processes would be influenced, as indicated in Ref. 13. Therefore, the term "gas concentration process" is introduced to encompass potentially more complicated gas transport processes.[14] When switching from nitrogen to helium, the LF_x process decreases in absolute value, resulting in a smaller contribution to the polarization resistance. The low-frequency processes LF_{1+2} (LF_1 + LF_2) also decrease.

In Fig. 5, the dependency of impedance on variation of hydrogen and steam partial pressure is shown. An increase in hydrogen partial pressure is associated with a decrease in ohmic resistance, LF_x (absolute value), and LF_{1+2} processes. The first is possibly attributed to the pO_2-dependency of the GDC structure accounting for conducting electrons in the inactive part of electrode. Conversely, the middle frequency (MF) process shows a weak dependency on hydrogen content. With an increase in water steam content, the LF_x process exhibits a strong negative dependency in absolute value, while LF_1 shifts to a higher frequency range and overlaps with LF_2 under high steam content (Figs. 5c, 5d). Due to strong overlapping,
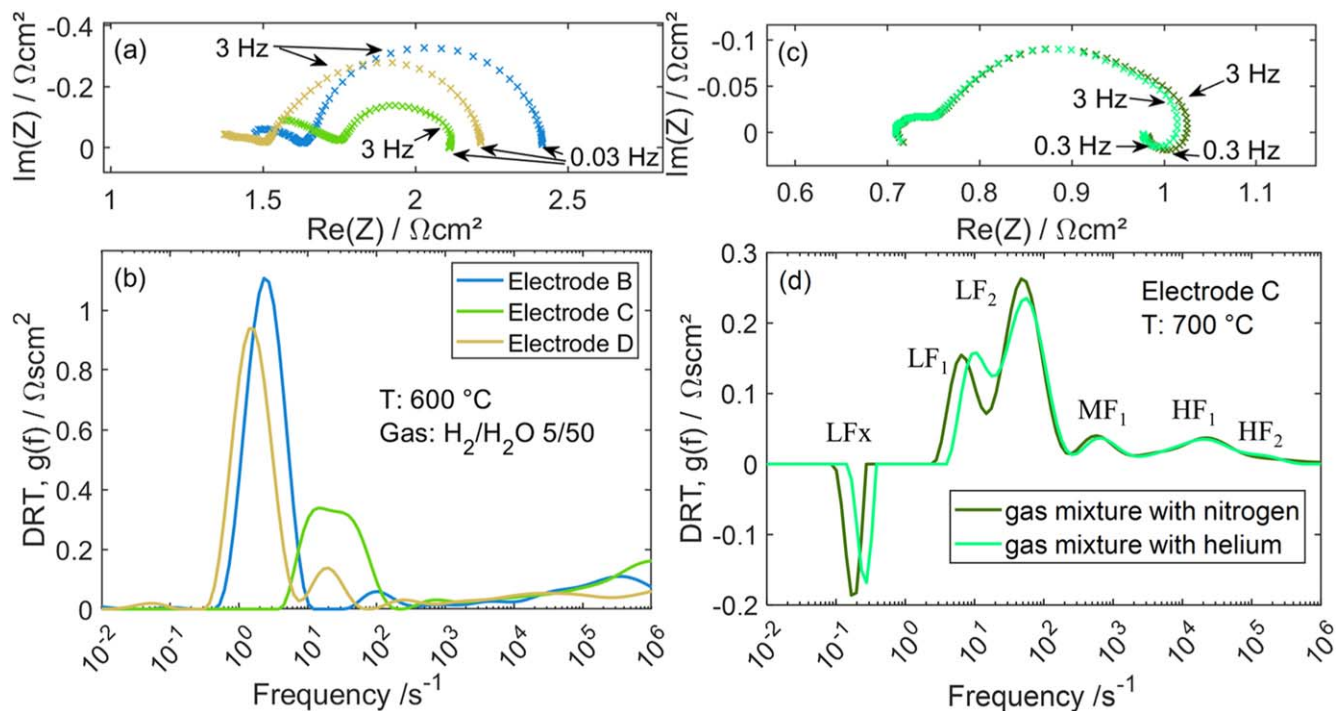
Figure 4. (a) Impedance spectra and (b) corresponding DRTs of electrode B-D at 600 °C with a gas mixture of steam: hydrogen of 50:50. (c) Impedance spectra and (d) corresponding DRTs of electrode C under different inert gases (steam and hydrogen partial pressures are 0.05 and 0.30 atm at 700 °C). The position of cells in the setup is shown in Fig. 2b. The values are halved for single electrode evaluation.
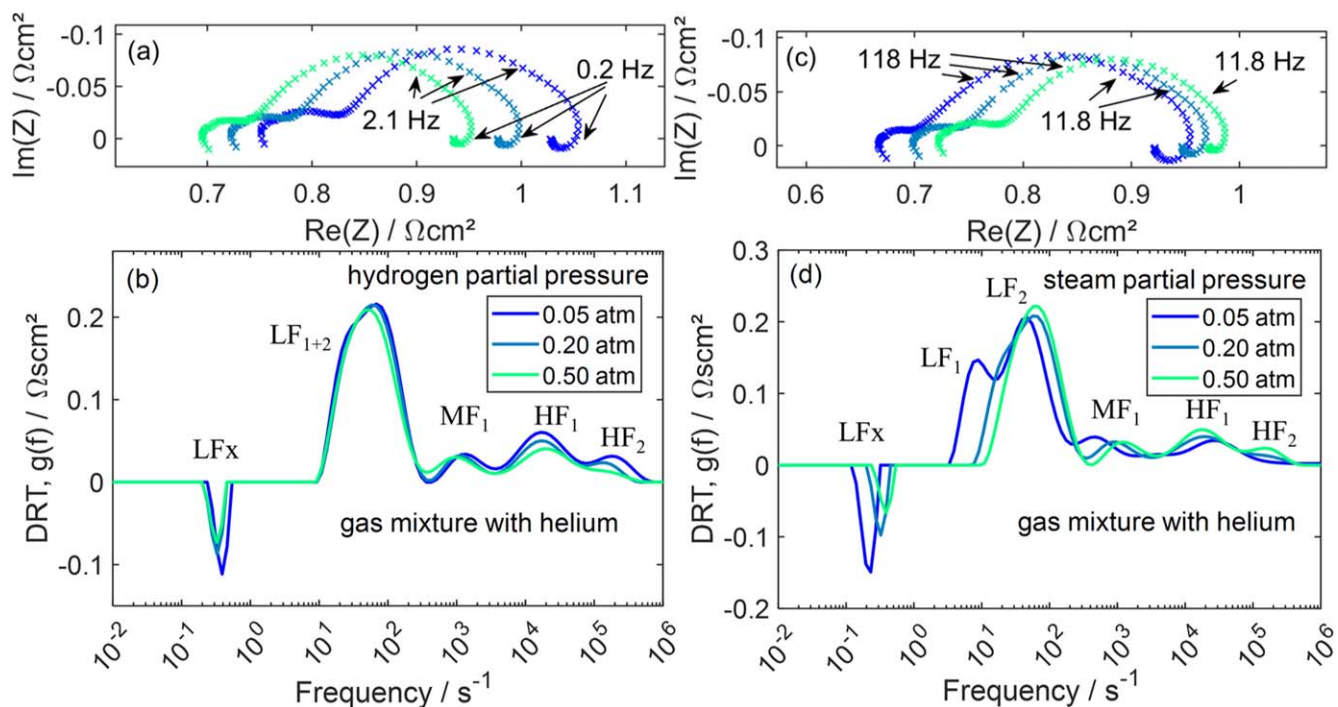
Figure 5. Impedance spectra and corresponding DRTs of electrode C at 700 °C with varying hydrogen partial pressure from 0.05–0.5 atm (a), (b), while keeping steam partial pressure constant at 0.30 atm and steam partial pressure from 0.05–0.5 atm (c), (d), while keeping hydrogen partial pressure constant at 0.30 atm. Helium is used as inert gas. The values are halved for single electrode evaluation.

the dependency of LF_1 and LF_2 on steam content cannot be conclusively commented upon, but the overall LF_{1+2} process decreases. In contrast, the MF process has a weaker dependency on steam content, although stronger than its dependency on hydrogen content.

Several new features have emerged in the impedance of electrode C compared to the widely reported results on Ni/GDC symmetrical cells tested in a single-cell setup in Ref. 8,12. Identifying and quantifying all processes are not the primary focus of this work. Considering the evaluation of the suggested testing methodology

with the active driven gas layer concept, the emphasis will be placed on understanding the physicochemical background of the observed low-frequency inductive loops and developing a model capable of reproducing this behavior.

The phenomenon of the pseudo-inductive loop at the low-frequency range is widely observed and reported in other electrochemical fields.[15–19] Theoretical research has linked such phenomena to electrochemical adsorption/desorption processes, such as side reactions with intermediate species.[20–26] Another common theory attributes it to metallic corrosion/dissolution.[27,28] In the field of SOCs, only a limited number of papers have discussed similar phenomena. For instance, T. Jacobsen et al.[29] observed such a phenomenon on Pt point electrodes on YSZ at 1000 °C and attributed it to a current-induced activation mechanism followed by deactivation at equilibrium conditions. Guillaume Jeanmonod[30] related the appearance of an inductive loop to possible modifications in electrochemical pathways due to the poisoning effects of chlorine on a solid oxide cell operated in co-electrolysis. Venkatesh Sarda[31] reported such a phenomenon on a Ni/YSZ anode half-cell, indicating a strengthening effect with increasing load. WG Bessler[14] suggested a possible occurrence of an inductive loop due to complex gas concentration loss, although this was not supported by experimental results.

Test in single- and multi-cell setup.—To gain a deeper understanding of the pseudo-inductive loop, it is necessary to test the cell with and without neighboring cells. Cell E was tested in a regular single-cell setup with a gas flow rate of 0.25 nlm per electrode (Fig. 2c) and between two cells of type A (where cell A performed worse than cell E) in the active driven gas layer (multi-cell) setup (Fig. 2d). The results are shown in Fig. 6. Due to differences in the test benches, the ohmic contribution is ignored, and the impedance at 10 kHz is set to 0 on real axis for direct comparison. The absence of the inductive loop when the cell is tested in the regular single-cell setup and the strong impact of the inert gas type on the low frequency inductive loop suggests that in case of the investigated cells, the inductive loop at low frequencies is related to the active driven gas layer concept and not to the cell itself.

A comparison of DRTs from tests in a multi-cell setup to tests in a single-cell setup (Fig. 6c) reveals an enlarged process LF_{1+2} between 1 and 10 Hz. Its impact on the overall polarization resistance is partly canceled out by the appearance of the pseudo-inductive loop exhibiting a negative contribution. Since the process LF_{1+2} depends on the type of inert gas, it could be assumed that gas transport-related processes are the primary contributors to this enlargement. Remarkably, the polarization resistance of electrode E is larger when measured in a multi-cell setup ($0.75 \, \Omega \cdot cm^2$) compared to a single-cell setup ($0.67 \, \Omega \cdot cm^2$) under identical testing conditions with helium as the inert gas. This is likely due to the enlarged low frequency processes LF_{1+2}, whose enlargement cannot be canceled out by the inductive loop. Consistent with findings in Ref. 8 the polarization resistance tends to decrease in gas mixtures containing helium in both experimental setups. The differences in polarization resistance are $0.05 \, \Omega \cdot cm^2$ (in the multi-cell test setup) and $0.08 \, \Omega \cdot cm^2$ (in the single-cell test setup), corresponding to gas diffusion losses of 0.0294 and $0.0473 \, \Omega \cdot cm^2$ at 800 °C with a 50:50 water steam to hydrogen gas mixture, respectively. Both values are larger than the values calculated for multi-cell and regular single-cell setup mentioned above. For the former, the appearance of the pseudo-inductive loop and possible more complex gas transport processes make a direct comparison challenging. For the latter, possible causes could partly be attributed to differences in cell structure, such as the presence of an extra-fine Ni structure (particle size < 10 nm) resulted from infiltration in electrode E.

Due to the absence of identification and quantification for all processes within the electrode, a detailed analysis of the results is challenging. The application of this new test method might introduce complex gas transport dynamics, such as gas transport resulted from a concentration gradient between two electrodes through the Ni-
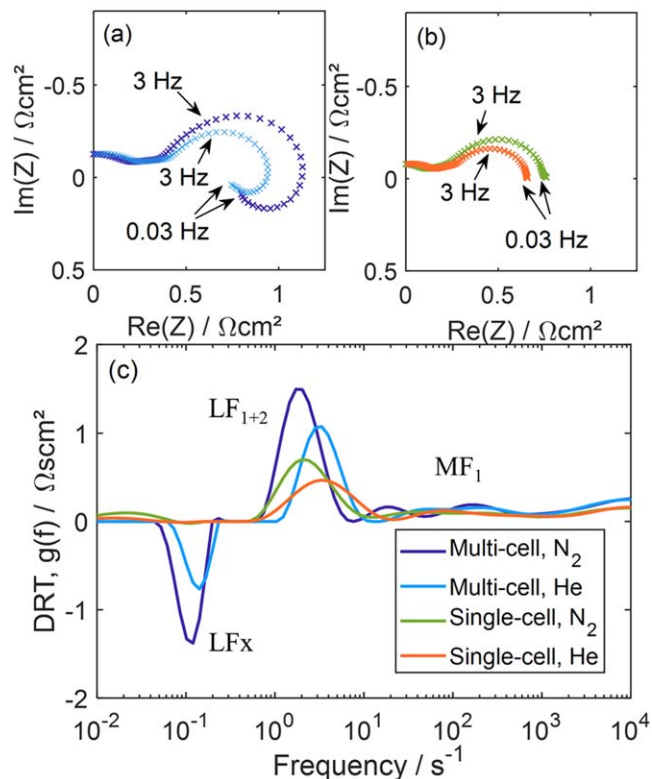

Figure 6. Impedance spectra of one electrode of cell E tested in (a) multi- and (b) single-cell test setup under different inert gases (steam and hydrogen partial pressures are 0.05 and 0.30 atm at 600 °C) and (b) corresponding DRTs.

mesh and the chamber's atmosphere to the space between the electrodes. Comprehending the origin of the pseudo-inductive loop requires a model that considers ac current flow, the related dynamics of production and consumption of reactants and reaction products, and the dynamic gas transport between two electrodes connected by the active driven gas layer. In the next section, we establish and discuss a simplified model to provide insights into these complexities and explain the occurrence of the low frequency inductive loop.

Modeling and simulations.—Multiple repetitions were carried out to test different cells in the multi-cell setup. The pseudo-inductive loop was only observed in spectra of cells exhibiting a much better electrochemical performance than their neighbors. This suggests a potential connection of such phenomenon to differences among the cells. When identical cells are assembled, as shown in Fig. 2a, the performances of neighboring cells tend to be similar and no inductive loops are observed.

A possible explanation for the observed behavior must be related to polarization resistance and chemical capacity of the two different electrodes of neighboring cells. Considering the simplest equivalent circuit model for an electrode, it consists of a charge transfer resistance (R_i) and a parallel capacity (C_i), as displayed in Fig. 7. In the case of the ac-current used for impedance measurements, the total supplied current provided by the impedance analyzer will split up at the electrode into 2 parts: one flowing through the charge transfer resistance whereas the other is "stored" in the (chemical) capacitance of the GDC in the electrode. The first part will result in the oxidation / reduction of gas species (H_2/H_2O) and thus affect the gas composition whereas the charge related to the second part is stored in the capacitance. In a more chemical way, oxygen ions coming via the 8YSZ-electrolyte might either pass the charge transfer resistance, react with hydrogen and affect the gas composition or be stored in the chemical capacity of the GDC and thus not interact with gaseous species in the Ni-mesh.
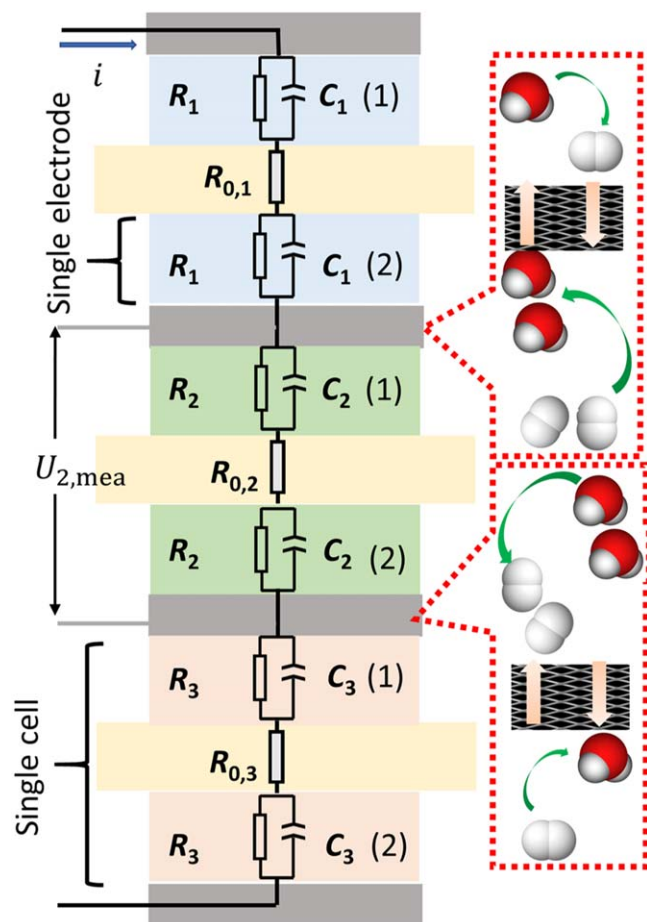
Figure 7. Schematic representation of the multi-cell test model with a simplified equivalent circuit. Current collector and associated nickel mesh and wires are depicted in grey, 8YSZ electrolytes in yellow, and the electrodes of cell 1–3 in blue, green and orange, respectively.

The equivalent circuit for one cell is simplified to two R∥C elements (resistance in parallel to a capacitance) representing charge transfer resistance and the chemical capacity of the Ni/GDC electrodes and an ohmic resistance R_0 representing losses related to ionic and electronic transport in the cell. The equivalent circuit for three cells assembled using the active driven gas layer concept consists of three such circuits in series, with Ni-meshes in between, whose resistance can be neglected.

The current flowing through the charge transfer resistances in identical electrodes connected via the active driven gas layer is thus identical, and it is proportional to the speed of fuel production/ consumption. Between these two electrodes separated by a nickel mesh, the hydrogen/water steam produced/consumed in a given time unit equals the hydrogen/steam consumed/produced at the other electrode (as indicated by the red dialog box in Fig. 1b). Assuming rapid gas transport in the nickel mesh and the porous electrodes, a minor gas concentration gradient between the electrodes can be continuously evened out and ignored. The atmosphere near the electrodes is therefore approximately the same as the preset gas mixture in the chamber and identical on both sides of one cell.

If neighboring electrodes exhibit different performances, the assumed quasi-equilibrium and symmetry is disrupted. As illustrated in Fig. 7, three different cells are arranged in series with only Ni-meshes in between their electrodes. The gas concentration process between two neighboring electrodes is assumed to be limited to perpendicular transport in the Ni-mesh (no in-plane exchange to chamber) and very fast. Thus, the gas compositions in the neighboring electrodes (e.g., position (2) of cell 1 and position (1) of cell 2

in Fig. 7) are identical. It is assumed that the chemical capacitance C_i, are of similar value for all 3 cells, as they depend on GDC-amount in the electrodes. Considering the electrode of cell 2 performs the best ($R_2 < R_1$, R_3), the ac-current flowing through the charge transfer resistances is thus largest on R_2. Assuming the current flowing through cell 1 to 3, the produced hydrogen in the position (2) of cell 1 is thus less than that consumed at the position (1) of cell 2. The consumed steam is also less than produced. Thus, in the assumed active driven gas layer, an excess of steam/ lack of hydrogen compared to the set atmosphere in the chamber occurs for a positive current amplitude. In contrast, at the position indicated by the second red dialog window in Fig. 7, there is an excess of hydrogen/ a lack of steam. Consequently, the performance wise better cell 2 in the center exhibits different gas compositions in its electrodes. The resulting Nernst voltage across cell 2 can be calculated using:

$$U_N = \frac{RT}{2F} \ln\left(\frac{\sqrt{p_{O_2,\text{bottom electrode}}}}{\sqrt{p_{O_2,\text{top electrode}}}} \right) \quad [1]$$

where R is the gas constant (8.314 J/(mol·K)), T is the absolute temperature (in Kelvin), 2 is the number of electrons transferred in the reaction, F is Faraday's constant (96,485 C mol^{-1}), $p_{O_2,\text{top electrode}}$ and $p_{O_2,\text{bottom electrode}}$ are the partial pressure of oxygen at the two electrodes of cell 2. The Nernst voltage of cell 2 would be zero if the gas compositions in both electrodes were identical (Fig. 1b). The unsymmetrical atmosphere across cell 2 (Fig. 7) results in a non-zero Nernst voltage U_N.

The measured voltage across cell 2 during the impedance measurement (ohmic resistance neglected) is:

$$U_{2,\text{mea}} = \frac{2R_2}{1 + j\omega R_2 C_2} \cdot i + U_N \quad [2]$$

where w denotes angular velocity (rad/s), i the sinusoidal current signal of the impedance analyzer (A), and j the imaginary unit.

The measured impedance of cell 2 is:

$$Z_{2,\text{mea}} = \frac{2R_2}{1 + j\omega R_2 C_2} + \frac{U_N}{i} \quad [3]$$

The detailed deduction and calculation process to simulate the impedance response in the investigated frequency range are illustrated in the appendix. Table II lists the relevant parameters for modeling the impedance of cell C in Fig. 2b under different gas compositions. I denotes the amplitude of ac-current., and p_{H_2O} the steam partial pressure preset in the chamber. These parameters were obtained by estimating the values with R∥C elements derived from the measured impedances of cells B, C, and D (corresponding to cells 1, 2, and 3 in Fig. 7) at 700 °C under the same atmosphere as shown in Figs. 5c, d. Since the measurements were not reliable due to known gas composition asymmetry in probably all three cells and to simplify the calculation process, the capacitances for all three cells are set to the same value as that of cell B, and the estimated resistance of cell B is applied in both cell 1 and 3. All ohmic resistances ($R_{0,i}$) are ignored (set to 0). The simulations were conducted using MATLAB®. The results are presented in Figs. 8a, b.

As depicted in Fig. 8a, a pseudo-inductive loop consistently emerged in all simulations. With increasing steam partial pressure, the inductive loop decreases in absolute value. The endpoint at the lowest frequency is shifted towards a higher value on the real axis, indicating an increase in polarization resistance. The capacitive semicircle at higher frequencies, which is representing the RC-behavior of the electrode, is affected at low pH$_2$O values. Although the splitting of LF$_{1+2}$ and the shift of LF$_x$ towards lower frequency ranges are not observed, the DRTs presented in Fig. 8b show that both LF$_x$ and LF$_{1+2}$ processes decrease with increasing steam partial pressure, consistent with the trend shown in Fig. 5d.
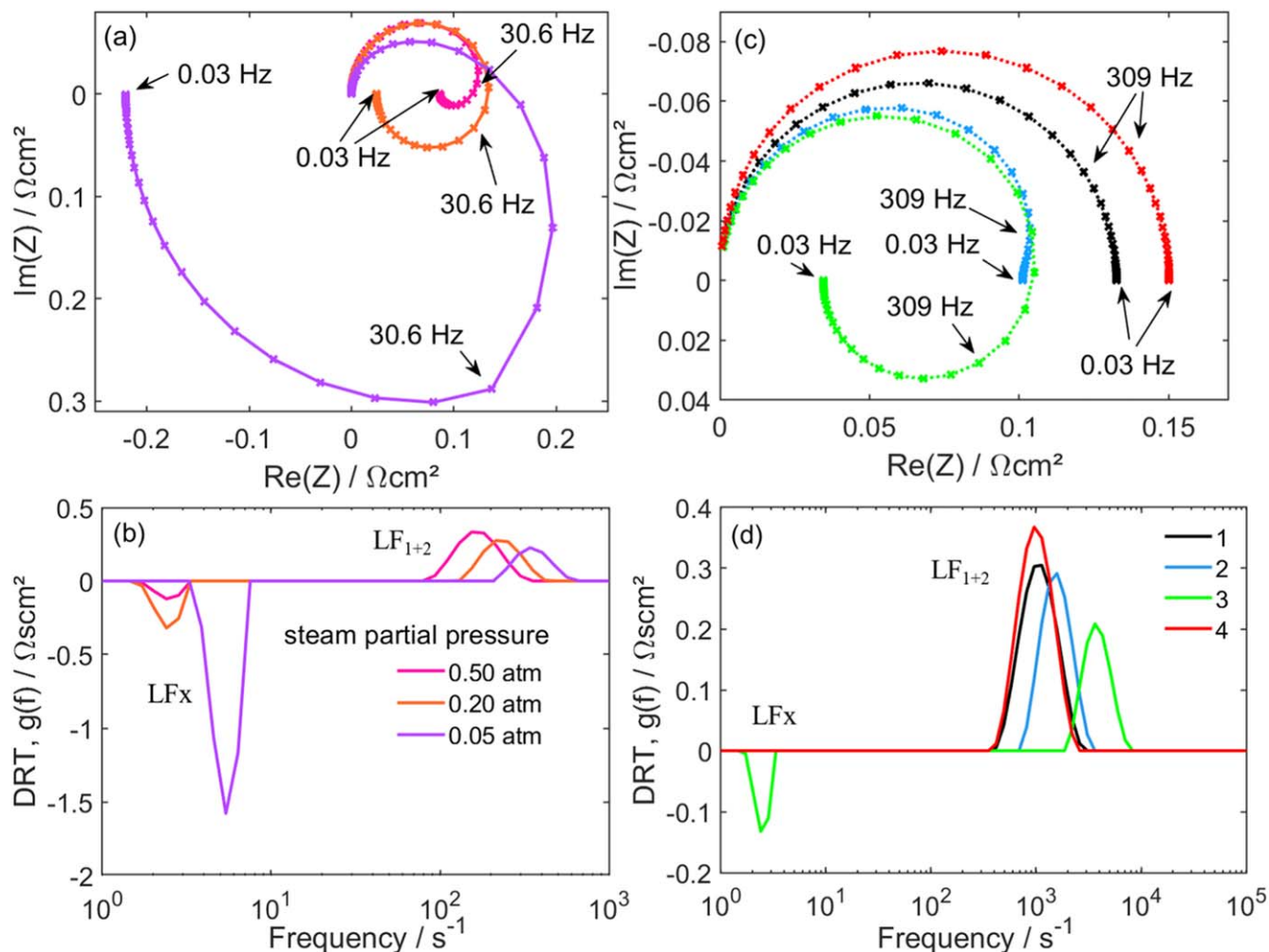
Figure 8. (a) Simulated impedances and (b) corresponding DRTs of cell C (Fig. 2b) at 700 °C under varying steam partial pressure from 0.05–0.5 atm, while keeping hydrogen partial pressure constant to be 0.30 atm with helium as inert gas. (c) Simulated impedance and (d) corresponding DRTs of cell 2 (Fig. 7) with varying neighboring cell performance.

Table II. Model parameters for the simulating impedance of the symmetrical anode cell tested in a multi-cell test setup with worse-performing neighboring cells at 700 °C under different steam partial pressure while keeping hydrogen partial pressure constant at 0.3 atm and with nitrogen as inert gas.

I (A)	p_{H_2O} (atm)	R_1, R_3 ($\Omega\cdot cm^2$)	C_i (F)	R_2 ($\Omega\cdot cm^2$)
0.024	0.05	0.45	0.090	0.24
	0.20	0.37	0.075	0.21
	0.50	0.33	0.069	0.18

However, the occurrence of a negative polarization resistance in the simulation was not observed in actual measurements. Furthermore, the impact of alternating inert gas types, as presented in Figs. 4c, d, cannot be elucidated by the established model, as gas diffusion is considered to be zero and no term in the model is representing the gas transport between two electrodes coupled by the active driven gas layer.

The deviation between simulated and measured results can be attributed to the simplified electrochemical model of the electrodes and the complex gas transport conditions, which were neglected in the aforementioned model. The dynamic gas transport between two neighboring electrodes due to gas concentration gradients, and between the chamber and the "sealed" space in Ni-mesh between two electrodes, will be influenced by the types of inert gases.

Furthermore, the chemical capacity of the GDC is modeled by an ideal capacity, neglecting nonlinearities and a different dynamic behavior resulting from oxygen ion diffusion in GDC.

In a single cell test with a standing gas atmosphere as well as in case of a gas flow in the channels, the gas acts as a capacitive volume that is partly consumed in the active part of the electrode (local gas conversion). This results in a concentration gradient in the gas phase extending over electrode, contacting or supporting layers and gas channels and a subsequent diffusion of the gaseous species. The local change in gas composition at the electrode/electrolyte interface in the active part of the electrode results in a change in Nernst potential. Combining diffusive gas transport and Nernst potential, a resistive/capacitive behavior that is usually modeled by an RC- or a Warburg-element is obtained.[13,32]

In the cell stack analyzed in this work, the electrode of the neighboring cell can provide/consume more gas species than consumed/produced by the electrode of the investigated cell. Thus, the diffusive transport of gaseous species is directed opposite. Subsequently the related resistance and capacitance become negative, resulting in the observed inductive loops.[33]

To further explore the influence of neighboring cell performance, the impedance of cell 2 in Fig. 7c was simulated while keeping R_2 constant and varying the values of R_1 and R_3. For simplicity, all chemical capacitances were chosen to be the same, and ohmic resistances set to 0. Relevant parameters for 4 cases are listed in Table III, and the simulation results are presented in Figs. 8c, 8d.

Table III. Model parameters for simulating impedance of the symmetrical anode cell tested in a multi-cell test setup with varying neighboring cells at 700 °C in a gas mixture of steam: hydrogen of 50:50.

Case	p_{H_2O} (atm)	p_{H_2} (atm)	I (A)	T (°C)	R_1 ($\Omega \cdot cm^2$)	R_2 ($\Omega \cdot cm^2$)	R_3 ($\Omega \cdot cm^2$)	C_i (F)
1	0.5	0.5	0.05	700	0.13	0.13	0.13	0.07
2					0.25	0.13	0.25	0.07
3					0.50	0.13	0.50	0.07
4					0.06	0.13	0.06	0.07

In case number 1, where all three cells have the same performance, the simulated impedance arc forms a perfect semicircle, and the polarization resistance of cell 2 is 0.26 Ω, corresponding to twice the value of charge transfer resistance R_2. As the values of R_1 and R_3 increase, the simulated arc deviates from a semicircle. In case 2, the low-frequency curve tends to bend backward to a smaller value on the real axis, resulting in a decrease in polarization resistance (0.20 Ω). The peak LF_{1+2} moves towards higher frequency range and shrinks. With further increases in the values of R_1 and R_3 to around 4 times of R_2, a pseudo-inductive loop appears in the low-frequency range (case 3), leading to a polarization resistance of 0.069 Ω. A corresponding peak LF_x related to the inductive loop appears in DRT and the peak LF_{1+2} further decreases. Another scenario, where cell 2 performs worse than cells 1 and 3 (case 4), is also considered, as depicted in red in Figs. 8c, 8d. This results in an increase in polarization resistance (0.30 Ω), and no inductive loop occurs in this situation.

Conclusions

A novel test methodology for SOFC aimed at saving both time and budget by enabling the simultaneous testing of multiple cells in a stack with active driven gas layers was applied to different cell types, yielding partly unexpected results.

Initial application of this methodology to identical cells demonstrated good reproducibility in both initial characterization and long-term results, validating its effectiveness. The observed differences of 6.46% regarding the ohmic resistance and 2.74% regarding the polarization resistance as well as minor differences in the DRT are in an expected range for handmade cells.

However, in case of simultaneous testing of cells differing in their performance (polarization resistance), the better performing cells exhibited an unexpected pseudo-inductive loop at the low-frequency range in the impedance spectra, which could not be reproduced in a regular test bench. Additional tests in single- and multi-cell setups revealed a strong impact of different gas conversion at the different electrodes. The resulting deviations in gas composition at both electrodes result in an additional dynamic cell voltage which is considered to be the reason for the inductive loop.

To model this behavior at low frequencies, a simplified equivalent circuit model extended by additional cell voltage terms related to dynamically varying gas composition at both electrodes was developed. Impedance simulations revealed the pseudo-inductive impedance behavior at low frequencies and were able to reproduce the experimental results qualitatively.

The active driven gas layer test methodology is proved excellent in simultaneous testing of multiple identical cells, improving statistics and saving huge budget in money and time. However, strict limitations need to be considered if non-identical cells are to be tested simultaneously. A difference in electrode performance leads to a deviation in gas composition across one cell, resulting in an additional time-dependent voltage term that can create an inductive loop in the impedance spectra and falsifies the measured polarization resistance. Our observations and modeling approach provide an understanding for one type of the widely witnessed pseudo-inductive loops in electrochemistry. Further investigations and a multiphysics model coupling electrochemical reactions and complex gas transport are needed to fully comprehend the observed impedance behavior.

Appendix

Based on the schematic illustration in Fig. 7, a simplified mathematical model for simulating the impedance of cell 2 tested in the multi-cell setup is established and detailed in this section. Several assumptions were made to simplify the derivation and calculation processes:

1. All cells are measured under OCV. The only current source comes from ac activation signal by the impedance analyzer for impedance measurement.
2. The thickness of electrodes ($\sim$10 μm) is neglected as the thickness of Ni-mesh (200 μm) is dominant.
3. The space between two neighboring electrodes is assumed to be "sealed" by the Ni-mesh during impedance measurement, thus no in-plane exchange to chamber is possible. At the beginning of the measurement, the atmosphere in the "sealed" space is the same as the preset atmospheric conditions in the chamber.
4. The "sealed" space has an area of 1 cm^2, corresponding to the active electrode area and thickness of 200 μm, the same as the thickness of Ni-mesh, and a porosity of 0.5.
5. The gas transport in the "sealed" space is assumed to be perpendicular and ultra-fast, thus no gas concentration gradient is present within this space.
6. At low frequencies, the data acquisition of impedance measurement was carried out via sampling. Thus, the simulated impedance will be integrated in one period and averaged to mimic the digital reading procedure.

The activation current for impedance measurement flowing through the cells is:

$$i = I \cdot e^{j\omega t} \qquad [A \cdot 1]$$

t represents the time.

Based on Kirchhoff's law, the current flowing through each charge transfer resistance is:

$$I_{R_1} = \frac{\frac{1}{R_1}}{\frac{1}{R_1} + j\omega C_1} \cdot I \cdot e^{j\omega t}$$

$$I_{R_2} = \frac{\frac{1}{R_2}}{\frac{1}{R_2} + j\omega C_2} \cdot I \cdot e^{j\omega t}$$

$$I_{R_3} = \frac{\frac{1}{R_3}}{\frac{1}{R_3} + j\omega C_3} \cdot I \cdot e^{j\omega t} \qquad [A \cdot 2]$$

The production/consumption of each gas component is proportional to the current flowing through the charge transfer resistance. In the case of ac-current, the location where hydrogen is consumed will produce hydrogen in the next half period. Thus, from this point onward, the position (1) or (2) in Fig. 7 only denotes the geometry and is no longer directly related to the redox reaction. Taking the position (2) of cell 1 as an example, the mole mass changing rate of hydrogen/steam is:

$$\frac{dm_{H_2,1.(2)}}{dt} = -\frac{dm_{H_2O,1.(2)}}{dt} = \frac{I_{R_1}}{2F} \quad [A\cdot3]$$

The change in hydrogen/ water steam mole mass is thus:

$$\Delta m_{H_2,1.(2)} = -\Delta m_{H_2O,1.(2)} = \int \frac{I_{R_1}}{2F} dt \quad [A\cdot4]$$

In analogous to it, in the position (1) of cell 2:

$$-\frac{dm_{H_2,2.(1)}}{dt} = \frac{dm_{H_2O,2.(1)}}{dt} = \frac{I_{R_2}}{2F} \quad [A\cdot5]$$

$$-\Delta m_{H_2,2.(1)} = \Delta m_{H_2O,2.(1)} = \int \frac{I_{R_2}}{2F} dt \quad [A\cdot6]$$

The net change of hydrogen/ steam mole mass in the "sealed" space between cell 1 and 2 is:

$$\Delta m_{H_2,12} = -\Delta m_{H_2O,12} = \Delta m_{H_2,1.(2)} + \Delta m_{H_2,2.(1)} \quad [A\cdot7]$$

Based on assumptions 2–4 and the ideal gas law, the total gas mole mass in the "sealed" space is:

$$m_{sealed} = A \cdot d \cdot \varepsilon \cdot \frac{P}{R \cdot T} \quad [A\cdot8]$$

A is the active area of the electrode (1 cm^2), d and ε the thickness of Ni-mesh (200 μm) and the porosity (0.5), and P the pressure of the gas mixture (same as the atmosphere in our setup).

The preset mole fractions of hydrogen and steam are x_{H_2} and x_{H_2O}. Therefore, the preset mole masses for each component are:

$$m_{H_2,preset} = m_{sealed} \cdot x_{H_2}$$
$$m_{H_2O,preset} = m_{sealed} \cdot x_{H_2O} \quad [A\cdot9]$$

The mole masses of hydrogen and steam between cell 1 and 2 during the impedance measurement are:

$$m_{H_2,12} = m_{H_2,preset} + \Delta m_{H_2,12}$$
$$m_{H_2O,12} = m_{H_2O,preset} + \Delta m_{H_2O,12} \quad [A\cdot10]$$

Following the same procedure, the gas composition between cell 2 and 3 can be obtained. Based on Eq. (1), the Nernst voltage across cell 2 can be calculated with the help of the law of mass action:

$$U_N = \frac{RT}{2F} \ln\left(\frac{m_{H_2O,23} \cdot m_{H_2,12}}{m_{H_2,23} \cdot m_{H_2O,12}}\right) \quad [A\cdot11]$$

The measured impedance of cell 2 based on Eq. (3) is:

$$Z_{2,mea} = \frac{2R_2}{1 + j\omega R_2 C_2} + \frac{RT}{2F \cdot I \cdot e^{j\omega t}} \ln\left(\frac{m_{H_2O,23} \cdot m_{H_2,12}}{m_{H_2,23} \cdot m_{H_2O,12}}\right) \quad [A\cdot12]$$

Based on assumption 6, the simulated impedance of cell 2 should be:

$$Z_{2,mea,sim} = \frac{\int_0^{\frac{2\pi}{\omega}} Z_{2,mea} \, dt}{\frac{2\pi}{\omega}} \quad [A\cdot13]$$

ORCID

Y. Liu ⓘ https://orcid.org/0000-0001-5333-8927
Y. Hu ⓘ https://orcid.org/0000-0003-2710-6529
N. H. Menzler ⓘ https://orcid.org/0000-0001-7091-0980
A. Weber ⓘ https://orcid.org/0000-0003-1744-3732

References

1. L. Blum, Q. Fang, S. M. Groß-Barsnick, L. B. de Haart, J. Malzbender, N. H. Menzler, and W. J. Quadakkers, *Int. J. Hydrogen Energy*, **45**, 8955 (2020).
2. A. Ploner, A. Hagen, and A. Hauch, *Fuel Cells*, **17**, 498 (2017).
3. A. Ploner, A. Hagen, and A. Hauch, *J. Power Sources*, **395**, 379 (2018).
4. M. Z. Khan, M. T. Mehran, R. H. Song, J. W. Lee, S. B. Lee, and T. H. Lim, *J. Power Sources*, **391**, 94 (2018).
5. F. Han, M. Lang, P. Szabo, C. Geipel, C. Walter, and R. Costa, *J. Electrochem. Soc.*, **171**, 054515 (2024).
6. G. A. Hughes, K. Yakal-Kremski, A. V. Call, and S. A. Barnett, *J. Electrochem. Soc.*, **159**, F858 (2012).
7. A. Weber, "Electrochemical impedance spectroscopy tutorial manuscript." *The 15th European Solid Fuel Cell Forum, Luzern, Switzerland* (2022).
8. C. Grosselindemann, N. Russner, S. Dierickx, F. Wankmüller, and A. Weber, *J. Electrochem. Soc.*, **168**, 124506 (2021).
9. Y. Liu, F. Wankmüller, M. Juckel, and A. Weber, *Fuel Cells*, **23**, 430 (2023).
10. D. Klotz, A. Weber, and E. Ivers-Tiffée, *Electrochim. Acta*, **227**, 110 (2017).
11. A. Schiefer, M. Heinzmann, and A. Weber, *Fuel Cells*, **20**, 499 (2020).
12. M. Riegraf, R. Costa, G. Schiller, K. A. Friedrich, S. Dierickx, and A. Weber, *J. Electrochem. Soc.*, **166**, F865 (2019).
13. V. Sonn, A. Leonide, and E. Ivers-Tiffée, *J. Electrochem. Soc.*, **155**, B675 (2008).
14. W. G. Bessler, *J. Electrochem. Soc.*, **153**, A1492 (2006).
15. S. K. Roy and M. E. Orazem, *J. Electrochem. Soc.*, **154**, B883 (2007).
16. N. Wagner and M. Schulze, *Electrochim. Acta*, **48**, 3899 (2003).
17. N. Wagner and E. Gülzow, *J. Power Sources*, **127**, 341 (2004).
18. T. Schulz, C. Weinmüller, M. Nabavi, and D. Poulikakos, *J. Power Sources*, **195**, 7548 (2010).
19. S. I. Pyun and Y. G. Ryu, *J. Power Sources*, **62**, 1 (1996).
20. B. P. Setzler and T. F. Fuller, *J. Electrochem. Soc.*, **162**, F519 (2015).
21. O. Antoine, Y. Bultel, and R. Durand, *J. Electroanal. Chem.*, **499**, 85 (2001).
22. M. Mathias, D. Baker, W. Gu, M. Murphy, and K. C. Neyerlin, *ECS Meeting Abstracts* (IOP Publishing)1519 (2006).
23. A. A. Franco and M. Tembely, *J. Electrochem. Soc.*, **154**, B712 (2007).
24. H. Kuhn, A. Wokaun, and G. G. Scherer, *Electrochim. Acta*, **52**, 2322 (2007).
25. S. K. Roy, M. E. Orazem, and B. Tribollet, *J. Electrochem. Soc.*, **154**, B1378 (2007).
26. D. A. Harrington and B. E. Conway, *Electrochim. Acta*, **32**, 1703 (1987).
27. C. Li, Z. Peng, and J. Huang, *J. Phys. Chem. C*, **127**, 16367 (2023).
28. R. D. Armstrong and M. Henderson, *J. Electroanal. Chem.*, **40**, 121 (1972).
29. T. Jacobsen, B. Zachau-Christiansen, L. Bay, and M. J. Jørgensen, *Electrochim. Acta*, **46**, 1019 (2001).
30. G. Jeanmonod, S. Diethelm, and J. Van herle, *J. Power Sources*, **506**, 230247 (2021).
31. V. Sarda, "Degradation phenomena in the anode side of solid oxide fuel cell (SOFC) stacks." *PhD Thesis*, (Faculty of Mechanical Engineering, RWTH Aachen University) (2016).
32. J. Nielsen, T. Jacobsen, and M. Wandel, *Electrochim. Acta*, **56**, 7963 (2011).
33. D. Klotz, *Electrochem. Commun.*, **98**, 58 (2019).